



Investigation and process optimization for magnetic abrasive finishing additive manufacturing samples with different forming angles

Peixin Zhu¹ · Guixiang Zhang¹ · Xiao Teng¹ · Jiajing Du¹ · Linzhi Jiang¹ · Haoxin Chen¹ · Ning Liu¹

Received: 29 June 2021 / Accepted: 15 September 2021 / Published online: 28 September 2021
© The Author(s), under exclusive licence to Springer-Verlag London Ltd., part of Springer Nature 2021

Abstract

The staircase effect, balling effect, and powder adhesion as well as other problems in additive manufacturing (AM) forming all lead to the poor uniformity and high roughness of the sample surfaces. Therefore, there exist differences in the physical and mechanical properties of the samples. In this paper, the spherical composite magnetic abrasive particles (MAPs) are used for magnetic abrasive finishing (MAF) experimental investigations and process optimization of the AM sample surface. According to the Box-Behnken design principle of the response surface methodology, the finishing effects of different process parameters (spindle speed, feed speed, and machining gap) of MAF on the samples prepared by selective laser melting (SLM) with different formed angles are studied, the quadratic regression equations are established, and the validity of the equations are assessed by ANOVA and 3D response surfaces. After that, MAPs with smaller size were selected for the fine MAF experiments with the optimized parameters. Finally, we found that the optimal parameters of MAF for the same material with different forming angles are similar, but the polishing time consumed is quite different. After the MAF experiments, the changes of the surface Vickers hardness, roughness (Ra), and microscopic morphology are analyzed. The surface roughness of each sample is reduced from the initial 4–10 μm to about 100 nm, and the diversities in hardness are also reduced. MAF significantly improves the defects of poor surface uniformity caused by inconsistent forming angles.

Keywords Magnetic abrasive finishing · Selective laser melting · Response surface methodology · Surface roughness · Vickers hardness · AlSi10Mg alloy

1 Introduction

Because aluminum alloy has a series of advantages, such as low density, high specific strength, strong corrosion resistance, easy thermal conductivity, good plasticity, and processing performance, it is always the main material for aviation, transportation, electrical, and other industries [1–5]. At present, high-complex thin-walled precision aluminum alloy castings have been used in aircraft structures, such as the internal reinforcement ribs, webs, particle separator front casing, and intake lip [6]. Since the patent of Hull CW using laser beam deposition of metal powder directly forms large metal parts in the 1980s [7], additive manufacturing (AM) has developed rapidly. AM cannot only achieve better light-weight design and improve the efficiency of materials and

energy use, but also manufacture complex mesh and honeycomb structures that are difficult to process by traditional manufacturing methods and satisfy the various requirements [8].

However, the AM parts have many problems such as anisotropy and poor surface quality, making them difficult to meet product performance requirements. The nature of the layered forming of AM leads to a staircase effect on the surface of the formed samples [9]. The schematic diagram of the staircase effect is shown in Fig. 1. In Fig. 1, the red dashed line is the outline of the model, and the black stepped solid line is the outline of actual samples. In addition, balling effect [10] and powder adhesion [11] in AM further exacerbate the variation in the micromorphology and reduce the surface uniformity. The surfaces with high roughness are prone to stress concentration, which in turn induces microcracks, greatly reduces the fatigue performance of parts [12]. On the contrary, the low roughness makes the parts have better friction performance, corrosion resistance, and longer fatigue life [13].

✉ Guixiang Zhang
zhangx@sdu.edu.cn

¹ School of Mechanical Engineering, Shandong University of Technology, Zibo 255000, China

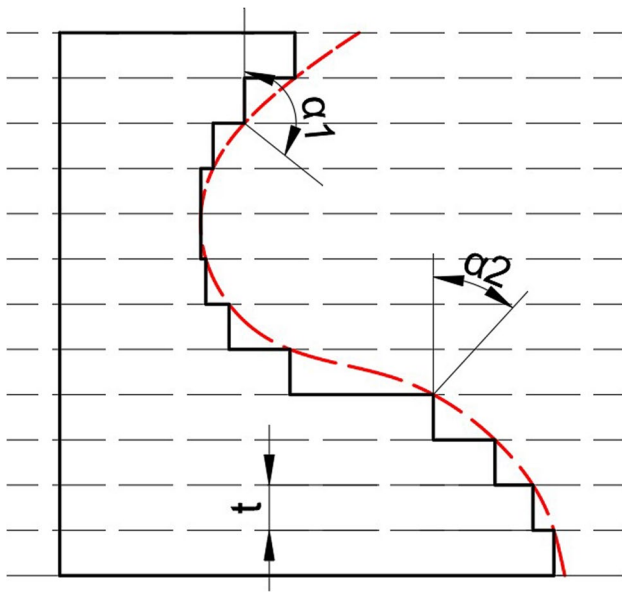


Fig. 1 Schematic diagram of staircase effect. t is the powder thickness and α is the forming angle of the surface

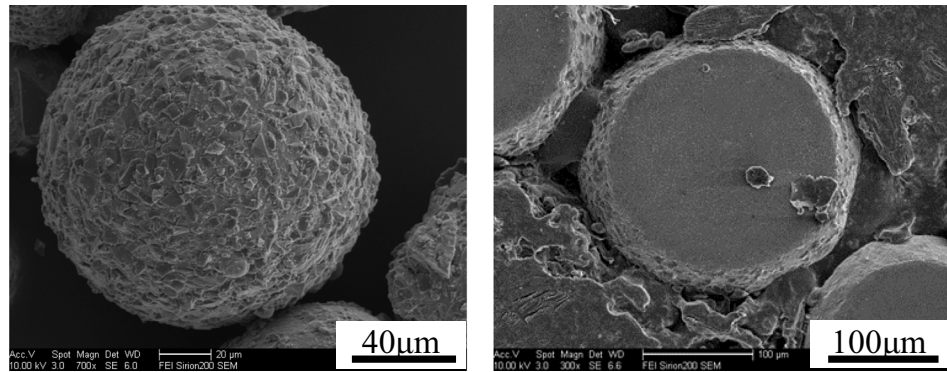
Advanced surface finishing technology is an effective way to improve the surface quality of complex structural parts. Beaucamp et al. used the shape adaptive grinding (SAG) to finish the free-form surface of the AM titanium alloy. After three times finishing, the final surface roughness reached below $Ra10$ nm [14]. Pyka et al. used a combination of chemical and electrochemical polishing to polish the porous structure stent and reduced the surface roughness Ra from $6 \sim 12$ μm before polishing to $0.2 \sim 1$ μm [15]. They argued that in this process, chemical polishing mainly quickly removes the metal powder adhering to the surface, and then electrochemical polishing further reduces the surface roughness [16]. Can Peng et al. carried out abrasive flow machining (AFM) experiments on AlSi10Mg parts additively manufactured. After AFM, compressive residual stress with the value of -30.5 ± 7.3 MPa is induced, and the surface roughness reduced from the initial Sa $13\text{--}14$ μm to the final 1.8 μm [17]. Bhaduri et al. used laser polishing (LP) to polish the AM aluminum alloys in a low-pressure environment with auxiliary ceramic heat insulation substrates. The average roughness Sa is reduced by about 80–88% [18].

Although the above-mentioned methods with various advantages have been used to try to solve the problem of subsequent surface polishing of AM parts, these methods also have some problems. The SAG is only suitable for continuous outer surfaces [12] and difficult to machine narrow grooves and inner surfaces. Chemical and electrochemical polishing are faced with the eternal problem of environmental protection. The cost of LP has been high, and the accessibility of LP to get to complex structures or inner surface is poor because of the nature of light propagation in a straight

line. Magnetic abrasive finishing (MAF) has the unparalleled advantage of accessibility on complex inner surfaces, but the uniformity of material removal is difficult to control, and there exists a problem of easy over-cutting at the edges. MAF is an effective processing method to improve the quality of workpiece surfaces, especially the irregular curved surfaces [19]. In the MAF process, the magnetic abrasive particles (MAPs) are bound by the magnetic field force to form a flexible magnetic abrasive brush with certain rigid characteristics. MAF is suitable for the polishing and deburring of complex free-form surfaces, internal cavities, and irregular-shaped parts. There have been precedents of scholars using MAF to polish AM components. Yamaguchi et al. through MAF reduced the roughness of 316L stainless steel formed by SLM exceeding Rz 100 to Rz 0.1 μm and further increased the residual compressive stress on the surface by replacing MAPs with $-50/+100$ mesh iron particles [20]. Guo et al. through a novel rotating-vibrating magnetic abrasive polishing method to finish a kind of complex internal surface which has a double-layered tube structure made by SLM of Inconel 718. The roughness was reduced from about Ra 7 μm to less than 1 μm [21]. Zhang et al. focused on the rapid removal instead of high precision of MAF SLM 316L stainless steel. They selected G50 steel grains, which with an average diameter of 500 μm and sharp edges, as the abrasive to polish the uneven surface produced by SLM. A maximum decrease of 75.7% in surface roughness Ra was achieved [22]. Zeng et al. carried out MAF experimental research on GH4169 (Inconel 718) alloy fuel injector formed by SLM. The roughness of the detected workpiece drops to 0.47 μm from the original 5.8 μm [23], but the MAPs they use are simple mechanical mixing or sintering abrasives, even only the iron matrix without abrasive phase, which have slow removal efficiency and poor polishing effect. In contrast, the MAPs used in this paper, prepared by gas atomization with rapid solidification, have high bonding strength between abrasive phase and matrix and high sphericity [24]. The morphology of MAPs is shown in Fig. 2. There are no Al_2O_3 particles in the MAPs, as shown in Fig. 2b, which maximizes the proportion of the iron matrix of MAPs, thereby ensuring that the abrasive is subjected to a greater magnetic field force in the magnetic field.

In this paper, we carry out MAF experiments of AlSi10Mg surfaces prepared by SLM with different forming angles. Our study aims to study the difference in MAF process of parts with different forming angles, and to optimize the process parameters through the response surface methodology (RSM). By using white light interferometer (MicroXAM-100, KLA-TENCOR Corporation, USA), 3D profiler (UP-Dule Mode, RETC, USA), metallurgical microscope (Axio Lab A, Carl Zeiss AG, Germany), and Vickers microhardness tester (DHV-1000Z, Shanghai Optical Instrument Fifth Factory

Fig. 2 SEM micrographs of Al₂O₃/Fe-based MAPs prepared by GARS. **(a)** MAPs outside morphology. **(b)** MAPs cross-sectional morphology



(a) MAPs outside morphology **(b)** MAPs cross-sectional morphology

Co., Ltd., China), we discussed the changes of morphology and Vickers hardness before and after MAF.

2 Experimental procedure

2.1 Experimental materials and samples forming

SLM® 125^{HL} (SLM Solutions GmbH, Germany) is selected as the AM forming equipment, as shown in Fig. 3. Figure 4 is the SEM micrograph of AlSi10Mg powder used in our SLM forming process. Implement SLM forming according to the parameters shown in Table 1. The parameters in Table 1 are the optimal parameters determined according to previous experiments [25]. The model of the sample is shown in Fig. 5a, and the blue parts are the supports. The samples formed by SLM are shown in Fig. 5b. Among the six workpieces (forming angle $\alpha=90, 100, 110, 120, 130, 140$), $\alpha=90$ is the control sample without staircase effect, and $\alpha=140$ is the exploratory test piece sample to study the removal ability of MAF for supports.

At room temperature (27 °C), by using Archimedes drainage method (Eq. 1) [26], the average density of the sample is measured to be $\rho_{\text{samp}} = 2.683 \pm 0.06 \text{ g/cm}^3$. Use the hardness tester to measure the hardness of the samples and the white light interferometer to measure the surface roughness. Considering that the initial roughness and the difference of roughness between different samples are large, which both causing the larger hardness measurement error or even difficulty to see the indentation, therefore, NO.100 sandpaper is used to reduce the surface roughness of the sample to about 2 μm before measuring the hardness. The applied load is 4.903 N, and the dwell time is 15 s. These data are all the average values of five measurements. The initial surface roughness (Ra) of each sample right side is shown in Fig. 6. $\alpha=140$ is unable to characterize its true roughness because of the residual support on the surface, which is not shown in Fig. 6.



Fig. 3 SLM@125HL equipment

$$\rho_{\text{samp}} = (\rho_{\text{alco}} - \rho_{\text{air}}) \cdot \frac{m_a}{m_{\text{air}} - m_{\text{alco}}} + \rho_{\text{air}} \quad (1)$$

where ρ_{alco} is the density of absolute ethanol, and ρ_{air} is the density of air. At room temperature 27 °C, $\rho_{\text{alco}} = 0.78352 \text{ g/cm}^3$ and $\rho_{\text{air}} = 0.001177 \text{ g/cm}^3$. m_a is the mass of the sample in the air, and m_{alco} is the mass of the sample in absolute ethanol.

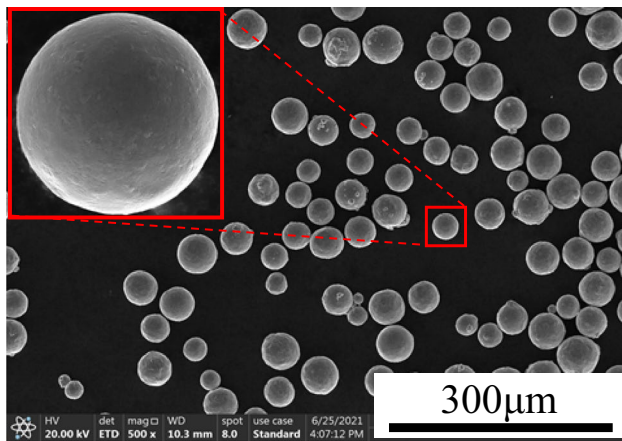


Fig. 4 SEM micrograph of the AlSi10Mg powder

Table 1 SLM AlSi10Mg forming parameters

Processing factors	Magnitude
Laser power (P)	250 W
Scan speed (v)	1600 mm/s
Layer thickness (h)	30 μm
Hatch spacing (d)	100 μm
Laser spot size	80 μm
Build chamber oxygen content	$\leq 0.1\%$
Platform temperature	200 $^{\circ}\text{C}$
scanning method	67 $^{\circ}$ rotating scan

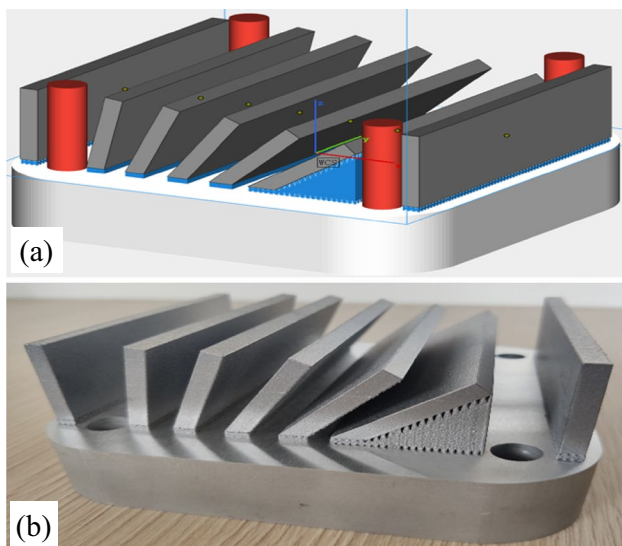


Fig. 5 3D model (a) and SLM forming sample (b)

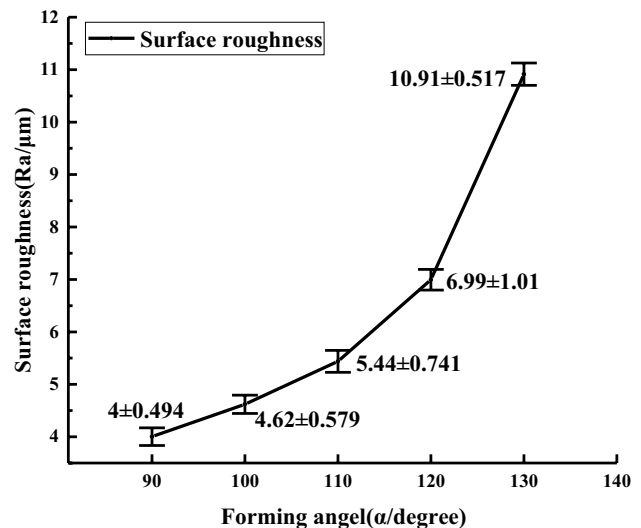


Fig. 6 Initial surface roughness (Ra) of SLM forming samples

2.2 The MAF system

The MAF system applied in the experiments is refitted from the XK7136C CNC milling machine, as shown in Fig. 7. Figure 7a is the physical picture of XK7136C CNC milling machine. Figure 7b is a photo taken during the MAF processing. Figure 7c is a schematic diagram of the modification section of the MAF system. Copper connecting rod is installed on the tool holder to connect the spindle with the magnetic pole. The workpiece is fixed on the workbench by a fixture, and the magnetic pole, after the MAPs is absorbed, is connected to the spindle through the copper connecting rod with two bolts, and then rotates with the spindle. Then, the trajectory control is carried out through the numerical control program to achieve the MAF process. Figure 7e and f are the physical map of the magnetic pole after the abrasive is adsorbed.

2.3 Response surface methodology and experimental setup

For each SLM forming part with different angles, according to the Box-Behnken design (BBD) principle of RSM [27], the spindle speed (A/rpm), feed speed ($B/\text{mm}\cdot\text{min}^{-1}$), and machining gap (C/mm) are independent variables, and the surface roughness (R_a) is the response value $Y(\alpha)$. A three-factor three-level response surface analysis test is performed. There were 17 groups in each experiment, including 5 central points for repeated tests to estimate the error. The test factors and levels are shown in Table 2. Other MAF processing conditions are shown in Table 3. After determining the optimal processing parameters through RSM, the finer MAPs (100–150 mesh) were selected to perform MAF of

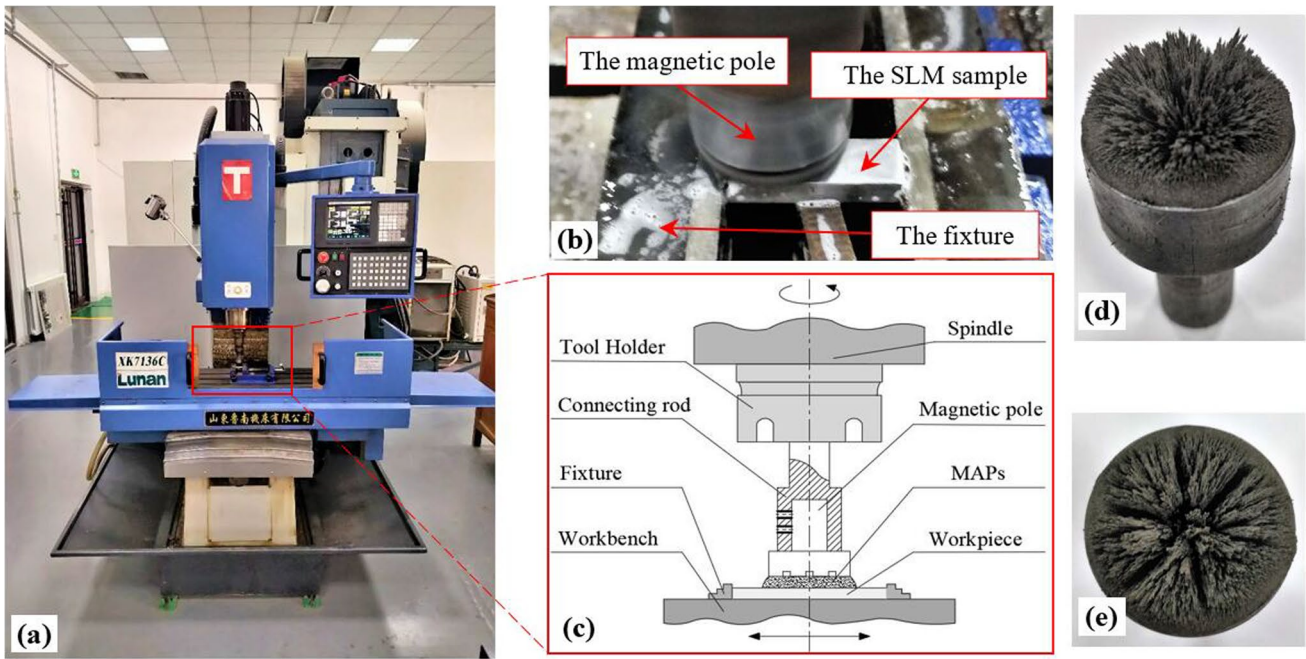


Fig. 7 The MAF system. (a) Physical diagram of MAF device. (b) MAF processing site. (c) Schematic diagram of the modification section. (d) The magnetic pole. (e) Top view of magnetic abrasive brush

Table 2 Factors and levels of RSM experiments

Level	Spindle speed (A/ rpm)	Feed speed (B/ mm•min ⁻¹)	Finishing gap (C/ mm)
-1	1500	10	1.5
0	1700	15	2.0
1	1900	20	2.5

Table 3 MAF process parameters

Experiment factors	Parameters
Material of magnetic pole	NdFeB N38
Size of magnetic pole	Φ25×13 mm
MAPs filling quality/g	2.0
MAPs/mesh	80–100
Abrasive particle phase size	W7 (5–7 μm)
Grinding fluid type (dosage)	Oil-based grinding fluid (3 ml/min)

the samples again. The finer MAPs have the small particle size, meaning a small proportion of the iron matrix, leading to a small magnetic field force. The scratches on the surface of the workpiece caused by finer MAPs are shallower compared with 80–100 mesh abrasive, which can achieve a better polishing effect.

3 Experimental results and discussions

3.1 Experimental results

After the first time MAF, the response value $Y(\alpha)$ of each workpiece at each level is shown in Table 4. The sample with $\alpha = 140^\circ$ is grinded with 600-mesh sandpaper to remove the support before MAF. From the results in the Table 4, the optimal roughness of each sample has little difference, all fluctuating around Ra 320 nm (bold data in Table 4). And for different samples, the best parameters for the MAF effect are $A = 1700$ n/min, $B = 15$ mm/min, and $C = 2$ mm, but the time consumed of MAF is different. The differences in MAF time consumption are shown in Fig. 8. Based on the initial roughness of 90° samples (about Ra 4 μm), we artificially divide the processing time into two parts. The negative semi-axis of the time axis is the time of MAF for the initial roughness to reach about 4 μm, that is, the $-T$. The positive semi-axis represents the time from 4 μm to the final roughness which no longer decreases, that is, the $+T$. For the $-T$ of Fig. 8, the differences in time consumption are largely due to the difference in initial surface roughness. For the $+T$, the time consumed increases as the forming angle increases. With the continuous progress of MAF, the material removal capacity of the brush becomes worse [19], and as the forming angle increases, the influence of the step effect becomes more obvious, result in the rasing in material removal. These factors both

Table 4 RSM setup of MAF and the result of $Y(\alpha)$

RUN	A	B	C	Y(90)	Y(100)	Y(110)	Y(120)	Y(130)	Y(140)
1	-1	0	-1	0.4481	0.4494	0.4572	0.4565	0.4573	0.4642
2	0	0	0	0.3271	0.3259	0.3272	0.3298	0.3245	0.3163
3	0	-1	-1	0.3794	0.3859	0.3883	0.385	0.3897	0.3915
4	0	1	-1	0.3897	0.3915	0.3974	0.3965	0.4042	0.3998
5	1	-1	0	0.4031	0.4077	0.4052	0.4054	0.4083	0.4121
6	-1	0	1	0.391	0.3912	0.3967	0.3966	0.4048	0.4038
7	0	0	0	0.3303	0.3317	0.3237	0.3289	0.3179	0.3266
8	1	0	-1	0.4673	0.4697	0.4717	0.4705	0.4774	0.4661
9	1	0	1	0.4142	0.4227	0.4208	0.4185	0.421	0.4257
10	0	0	0	0.3137	0.3192	0.3201	0.3174	0.3287	0.3311
11	1	1	0	0.4067	0.4081	0.4112	0.4105	0.4151	0.4198
12	0	1	1	0.3633	0.3644	0.3693	0.3688	0.3724	0.3761
13	-1	-1	0	0.3641	0.3729	0.372	0.3685	0.374	0.3723
14	-1	1	0	0.3836	0.3882	0.3859	0.3859	0.3929	0.3934
15	0	0	0	0.3264	0.3282	0.3336	0.3164	0.3098	0.3308
16	0	0	0	0.3271	0.3306	0.3238	0.3329	0.3241	0.3179
17	0	-1	1	0.3276	0.3344	0.336	0.3326	0.339	0.3404

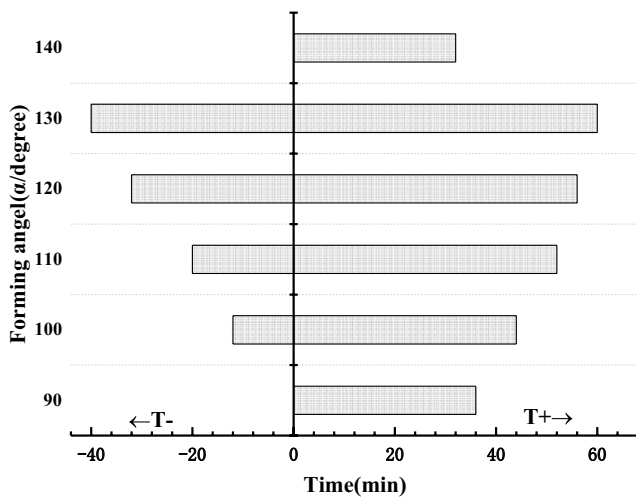


Fig. 8 Time consumed for MAF

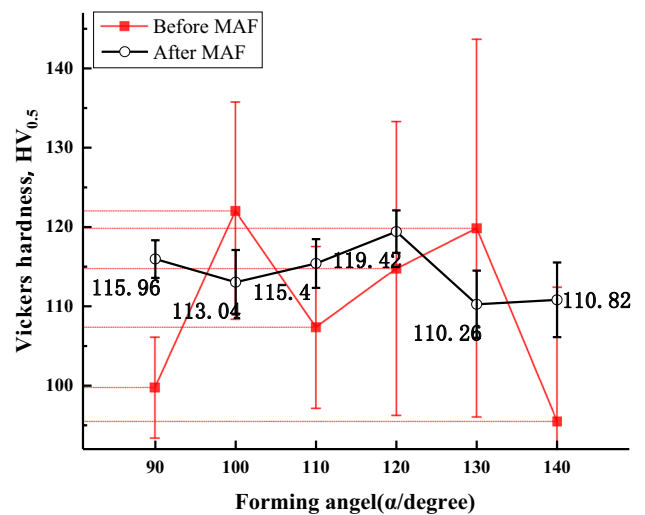


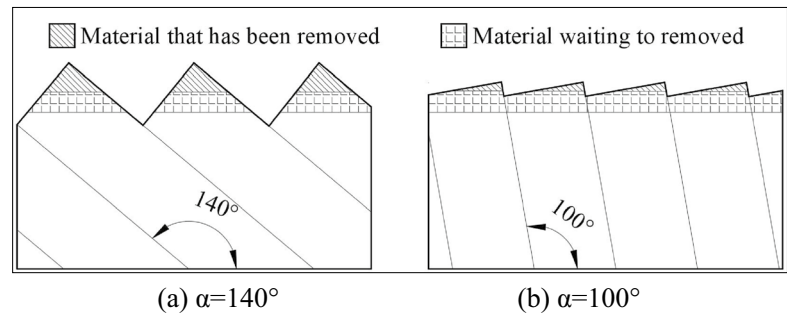
Fig. 9 Schematic diagram of the difference in material removal caused by staircase effect of SLM. (a) $\alpha = 140^\circ$. (b) $\alpha = 100^\circ$

lead to an increase in the time consumption of MAF, as shown in Fig. 9. The hardness before and after MAF of each sample with different forming angles is shown in Fig. 10. The hardness of each sample before MAF is different, which is caused by the difference in surface roughness and the difference in micromorphology. After MAF, because the surface roughness of each sample tends to be similar since the surface microscopic morphology is similar, the roughness difference is significantly reduced. This change is what we want to see during the MAF, which shows that MAF can significantly reduce the hardness difference caused by inconsistent forming angles.

3.2 ANOVA results of RSM

The ANOVA results of the six RSM models are shown in Table 6 in the Appendix at the end of this article. The p -values of the models are all much less than 0.0001, which indicates that the models are statistically significant. And the p values of the primary terms A , B , and C and the secondary terms A^2 and C^2 are less than 0.05, indicating that these terms have a significant impact on the response value. The p values of the interaction terms AB , AC , and BC are all greater than 0.05, indicating that the impact of the interaction response value is not significant; that is, the three

Fig. 10 Hardness change before/after MAF



factors have no interaction effect on the response value. The model’s lack-of-fit terms are all greater than 0.05, and the general requirement is greater than 0.1. The *p*-values of the six models lack-of-fit terms are all greater than 0.1, which is beneficial to the model and indicates that there is no lack of fit factors, so these regression equations can be used instead to analyze the experimental results at the real points of the test. The coefficient of variation (C.V.%) is less than 15%, indicating that there is no abnormal data. The difference between the corrected coefficient of determination *R*² (adj) and the predicted coefficient of determination is less than 0.2, and both are greater than 0.8, indicating that the coefficients are valid, and the results of calculations only 2.83%, 1.65%, 2.18%, 3.35%, 2.37%, and 3.26% errors cannot explain the actual model. The coefficient of variation of less than 15% and the coefficient of determination of correction close to unity further indicate that the model fits well and can be used for preliminary analysis of the process of the AISi10Mg samples with different forming angles of MAF [27, 28].

From the relationship of the mean square error of the single term, the selected three factors have an impact on the response value in descending order: machining gap (*C*), spindle speed (*A*), and feed speed (*B*). The source of the force in MAF is the magnetic field force. If the gap is too large, the magnetic field intensity on the surface of the samples will decrease, which will reduce the magnetic restraint of MAPs, and the flexibility of the abrasive brush will be increased, and the magnetic abrasive brush will lose the finishing ability. If the gap between the pole and sample is too small, the gap can contain a few MAPs, the fluidity of the magnetic abrasive brush becomes poor, and the rigidity is too large. Therefore, the finishing ability of the magnetic abrasive brush can only be guaranteed under a suitable gap. In summary, the machining gap has the greatest impact on the response value *Y* (α).

Next, we diagnose the reliability of the model from the perspective of visualization, that is, through the normal distribution of residuals, residuals vs predicted and residuals vs actual, as shown in Appendix Table 7. The normal distribution of the residuals, that is, the first column of pictures in Table 7, is basically on a straight line. The residuals vs

predicted graph, the second column, has points randomly distributed. The above two indicate that the standardized residual has nothing to do with the predicted value and prove that the fitted quadratic regression equation is effective. The picture in the third column of Table 2 is the comparison between the predicted value and the actual value. The actual value obtained from the experiment and the predicted value of the model are basically on the same straight line, which further shows that the obtained regression equation is highly consistent with the actual situation.

As mentioned earlier, the test coefficients of the interaction terms are all greater than 0.05, indicating that the interaction terms have no obvious influence on the response value. It can also be seen from Appendix Table 8 that the contours of the response surface projection do not appear to be closed and elongated ellipse and there is no very steep change in the response surface, further verifying that the interaction term has basically no effect on the response value.

$$Y(\alpha) = \beta_0 + \beta_1 \cdot A + \beta_2 \cdot B + \beta_3 \cdot C + \beta_4 \cdot AB + \beta_5 \cdot AC + \beta_6 \cdot BC + \beta_7 \cdot A^2 + \beta_8 \cdot B^2 + \beta_9 \cdot C^2 \quad (2)$$

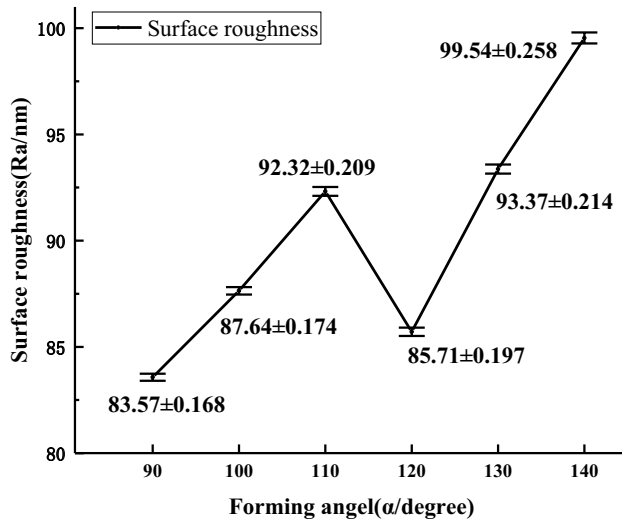
The coefficients of the equations in terms of coded established by RSM are shown in Table 5. The coded equations in the form of Eq. 2 are useful for identifying the relative impact of the factors by comparing the factor coefficients [29]. Among them, the *p* values of quadratic terms *AB*, *BC*, *AC*, and *B*² are all greater than 0.05, which is not significant, so these terms are finally discarded. Finally, Eq. 3 is obtained.

$$Y(\alpha) = 0.325 + 0.012 \cdot A + 0.008 \cdot B - 0.023 \cdot C + 0.067 \cdot A^2 + 0.044 \cdot C^2 \quad (3)$$

In summary, the optimal processing parameters of each angle forming sample obtained through the software are not very different. Combined with the actual situation of the processing system, rounded to *A* = 1700 n/min, *B* = 15 mm/min, and *C* = 2.2 mm. After determining the optimal processing parameters, we replaced the finer-grained abrasive for the second MAF of the workpiece and finally reduced the surface roughness to below 100 nm.

Table 5 RSM model coefficients

α	β_0	β_1	β_2	β_3	β_7	β_9
90	0.320	0.013	0.009	-0.024	0.065	0.040
100	0.330	0.013	0.006	-0.023	0.066	0.040
110	0.330	0.012	0.008	-0.024	0.066	0.045
120	0.330	0.012	0.009	-0.024	0.066	0.044
130	0.321	0.012	0.009	-0.024	0.070	0.049
140	0.320	0.011	0.009	-0.022	0.069	0.046
Ave	0.325	0.012	0.008	-0.023	0.067	0.044

**Fig. 11** Surface roughness (Ra/nm) and error bar after fine MAF

The specific values and errors are shown in Fig. 11. Compared with the initial roughness (Ra), not only the numerical value is significantly reduced, but the uniformity of roughness value is also significantly improved. This is the same as the change in hardness, which shows that MAF can significantly reduce the roughness difference caused by inconsistent forming angles.

When processing the same material, the processing parameters have little effect on the forming samples with different forming angles. To reduce the difficulty of programming and reduce the program statements, we can consider using the same parameters to process the forming surfaces with different forming angles. However, the processing time is different, which can be considered when writing the CNC machining program.

3.3 Morphology analysis before and after MAF

Figure 12 shows the morphology of initial, rough MAF, and fine MAF. Because the initial surface was too rough to take pictures by the white light interferometer, the RTEC 3D

profiler was used to observe the morphology of initial surface. The roughness after MAF is significantly reduced, so the white light interferometer with higher precision is used to analyze the morphology. From the 3D micromorphology, it can be seen more intuitively that the surface roughness has been greatly reduced, and the surface uniformity has also been significantly improved. Figure 13 shows the finely ground surface of the SLM sample observed through the metallurgical microscope. Figure 14 include photos of the surface of the initial, rough, and fine MAF. After fine MAF, the improvement of the mirror effect is very significant. What needs additional explanation here is the picture on the left side of the second row of Fig. 12f. This picture shows the surface of the MAF without removing the support. The support has not been completely removed. This is because the flexible magnetic abrasive brush is adaptive; it is difficult to effectively remove particularly sharp residual supports. Figure 14(f2.2) is the MAF after grinded with 600-mesh sandpaper. Compared with Fig. 14(f2.1), it has a foggy mirror effect. Therefore, for surfaces with supports, to improve the quality and efficiency of processing, other methods should be used in advance to remove the remaining supports.

4 Conclusions

1. The results in this study show that MAF can effectively improve the surface quality of the AM sample, the optimal surface parameters of the sample with different forming angles are not much different, but different processing time need to be set for different forming angles to ensure processing surface uniformity.
2. MAF can significantly reduce the differences in micro-morphology, roughness, hardness, and other aspects caused by different forming angles before processing and effectively improve the surface uniformity of the AM samples.
3. It has been verified by experiments that MAF has limited support removal ability in SLM forming. It is necessary to adjust the position of the forming part to reduce the contact area between the support and the forming part or to remove the surface support through pretreatment.

Fig. 12 3D morphology of the SLM samples (from top to bottom, X_1 , X_2 , and X_3 correspond to the sample surface of initial, rough MAF, and fine MAF, respectively). (a) $\alpha=90^\circ$, (b) $\alpha=100^\circ$, (c) $\alpha=110^\circ$, (d) $\alpha=120^\circ$, (e) $\alpha=130^\circ$, (f) $\alpha=140^\circ$

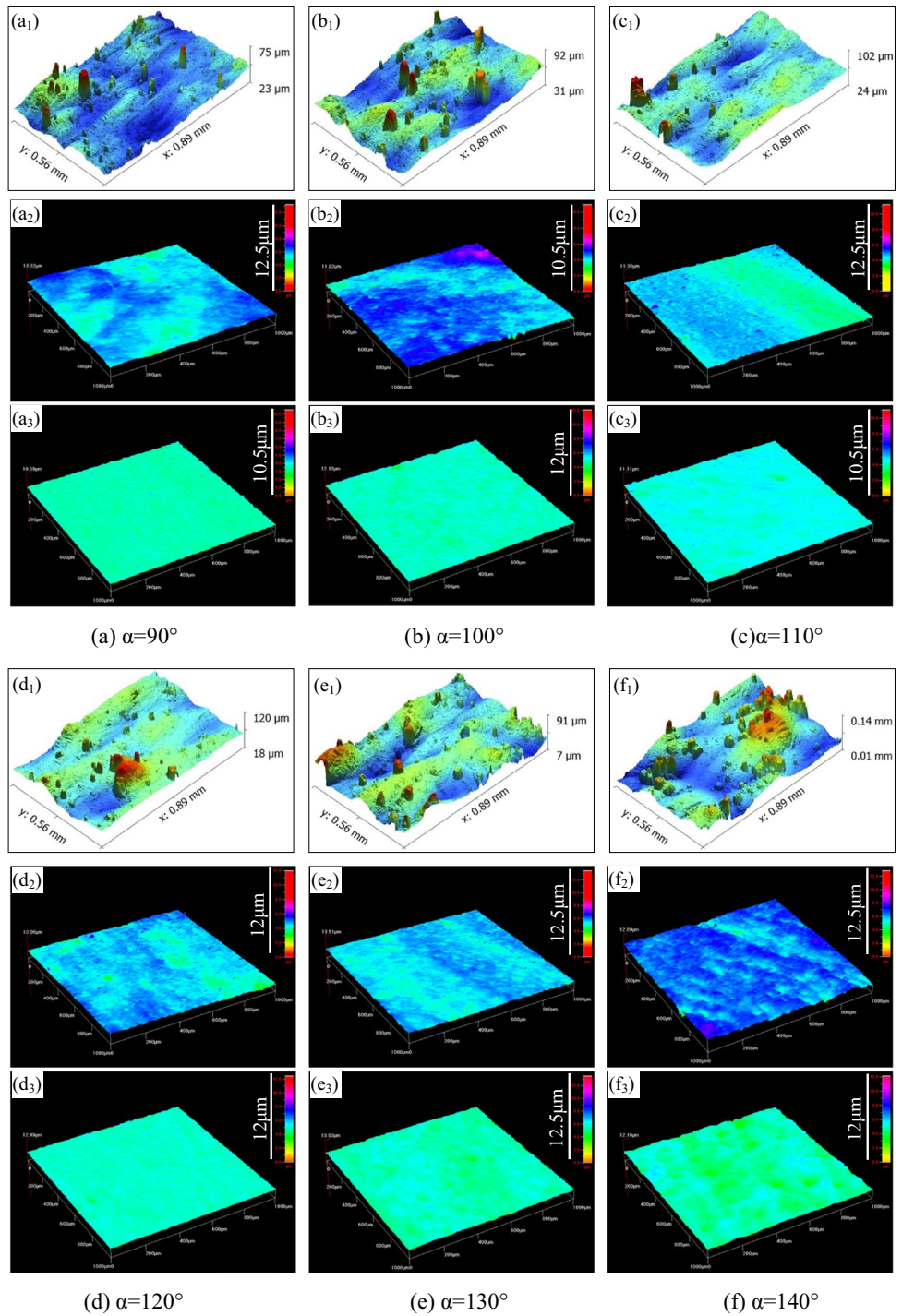


Fig. 13 Morphologies of the samples observed by the metallographic microscope. (a) $\alpha=90^\circ$, (b) $\alpha=100^\circ$, (c) $\alpha=110^\circ$, (d) $\alpha=120^\circ$, (e) $\alpha=130^\circ$, (f) $\alpha=140^\circ$

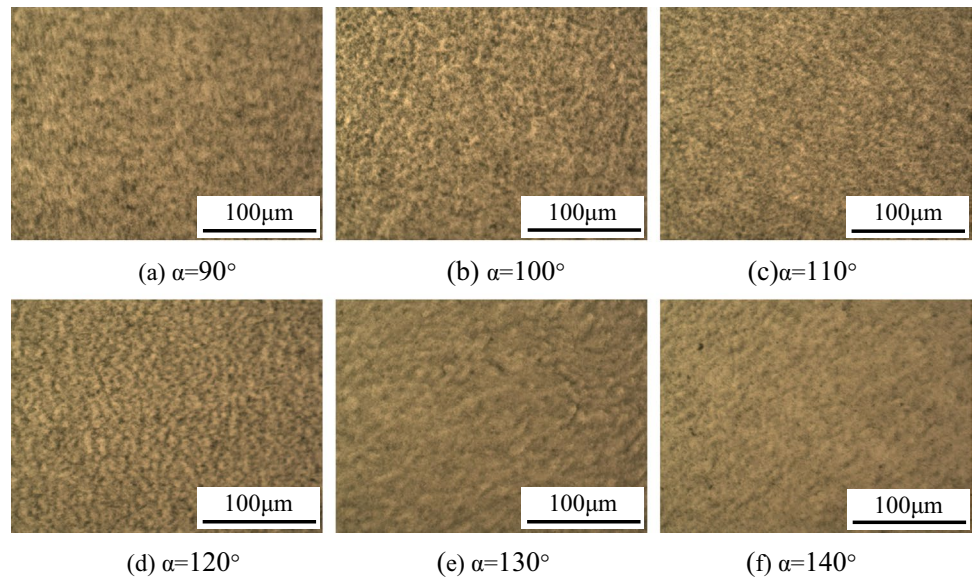
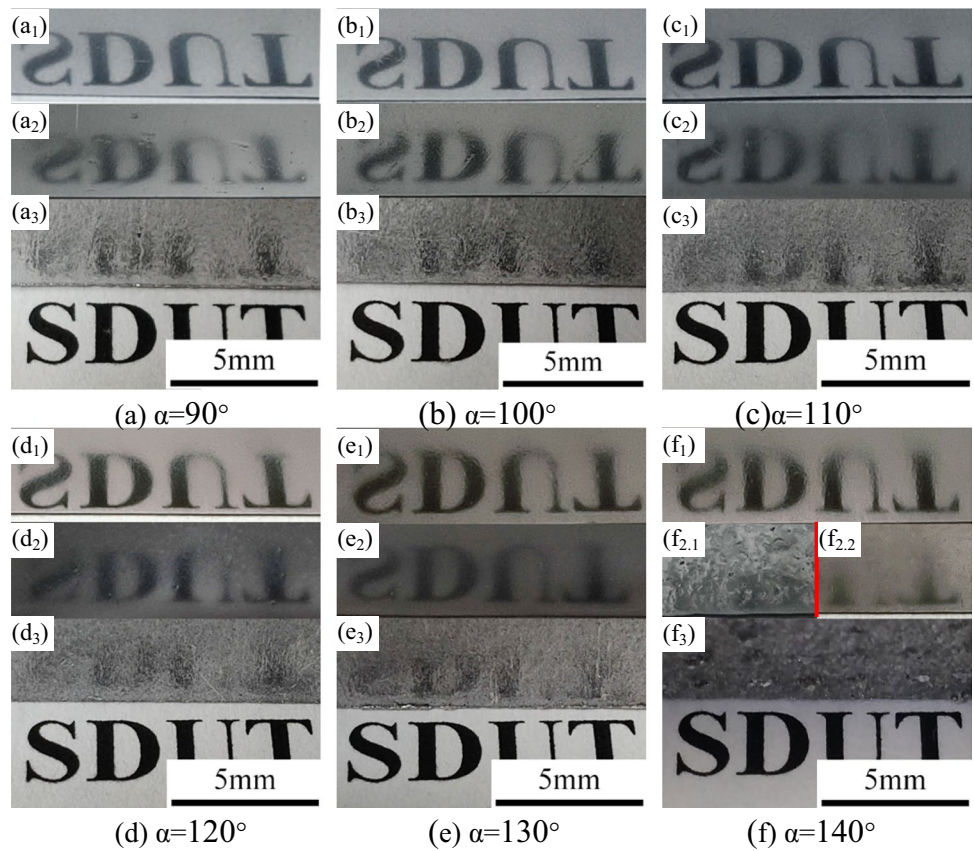


Fig. 14 Physical picture of Mirror effect (from top to bottom, X_1 , X_2 , and X_3 correspond to the sample surface of fine finishing, rough finishing, and initial, respectively. In (f), that is $\alpha=140^\circ$, the picture on the right ($f_{2,2}$) of the rough finishing surface is MAF after removing the support with sandpaper; the left ($f_{2,1}$) is directly MAF). (a) $\alpha=90^\circ$, (b) $\alpha=100^\circ$, (c) $\alpha=110^\circ$, (d) $\alpha=120^\circ$, (e) $\alpha=130^\circ$, (f) $\alpha=140^\circ$



Appendix

Table 6 ANOVA results for optimization of SLM samples with MAF

Source	Sum of squares	Mean square	F value	p value
(a) ANOVA results for optimization of MAF/Y (90)				
Model	0.033	3.62E-03	61.96	<0.0001
A spindle speed	1.37E-03	1.37E-03	23.39	0.0019
B feed rate	5.97E-04	5.97E-04	10.23	0.0151
C machining gap	4.44E-03	4.44E-03	76.01	<0.0001
AB	6.32E-05	6.32E-05	1.08	0.3327
AC	4.00E-06	4.00E-06	0.069	0.801
BC	1.61E-04	1.61E-04	2.76	0.1404
A ²	0.018	0.018	302.92	<0.0001
B ²	5.08E-07	5.08E-07	8.71E-03	0.9283
C ²	6.88E-03	6.88E-03	117.9	<0.0001
Residual	4.09E-04	5.84E-05		
Lack of fit	2.42E-04	8.07E-05	1.94	0.2652
Pure error	1.67E-04	4.16E-05		
Cor Total	0.033			
R-squared	0.9876	Adeq precision	24.036	
Adj R-squared	0.9717	C.V. %	2.04	
Pred R-squared	0.8746	PRESS	4.13E-03	
(b) ANOVA results for optimization of MAF/Y (100)				
Model	0.033	3.64E-03	107.21	<0.0001
A spindle speed	1.42E-03	1.42E-03	41.79	0.0003
B feed rate	3.29E-04	3.29E-04	9.7	0.017
C machining gap	4.22E-03	4.22E-03	124.48	<0.0001
AB	5.55E-05	5.55E-05	1.64	0.2416
AC	3.14E-05	3.14E-05	0.92	0.3683
BC	1.49E-04	1.49E-04	4.39	0.0745
A ²	0.018	0.018	534.98	<0.0001
B ²	8.88E-06	8.88E-06	2.60E-01	0.6246
C ²	6.90E-03	6.90E-03	203.36	<0.0001
Residual	2.38E-04	3.39E-05		
Lack of fit	1.39E-04	4.63E-05	1.88	0.2736285
Pure error	9.85E-05	2.46E-05		
Cor total	0.033			
R-squared	0.9928	Adeq precision	31.255	
Adj R-squared	0.9835	C.V. %	1.54	
Pred R-squared	0.9279	PRESS	2.38E-03	
(c) ANOVA results for optimization of MAF/Y (110)				
Model	0.035	3.88E-03	80.75	<0.0001
A spindle speed	1.18E-03	1.18E-03	24.51	0.0017
B feed rate	4.85E-04	4.85E-04	10.09	0.0156
C machining gap	4.60E-03	4.60E-03	95.65	<0.0001
AB	1.56E-05	1.56E-05	0.32	0.5867
AC	2.30E-05	2.30E-05	0.48	0.5111
BC	1.46E-04	1.46E-04	3.05	0.1245
A ²	0.018	0.018	380.02	<0.0001
B ²	1.72E-05	1.72E-05	3.60E-01	0.5683
C ²	8.54E-03	8.54E-03	177.72	<0.0001
Residual	3.37E-04	4.81E-05		
Lack of fit	2.33E-04	7.76E-05	3	0.1583
Pure error	1.04E-04	2.59E-05		
Cor total	0.035			
R-squared	0.9905	Adeq precision	27.197	
Adj R-squared	0.9782	C.V. %	1.83	
Pred R-squared	0.8898	PRESS	3.89E-03	
(d) ANOVA results for optimization of MAF/Y (120)				
Model	0.035	3.88E-03	52.22	<0.0001

Table 6 (continued)

Source	Sum of squares	Mean square	F value	<i>p</i> value
A spindle speed	1.19E-03	1.19E-03	15.96	0.0052
B feed rate	6.16E-04	6.16E-04	8.29	0.0237
C machining gap	4.61E-03	4.61E-03	62.02	0.0001
AB	3.78E-05	3.78E-05	0.51	0.4986
AC	1.56E-05	1.56E-05	0.21	0.6606
BC	1.53E-04	1.53E-04	2.05	0.195
A^2	0.018	0.018	247.98	<0.0001
B^2	7.65E-06	7.65E-06	0.1	0.7577
C^2	8.26E-03	8.26E-03	111.21	<0.0001
Residual	5.20E-04	7.43E-05		
Lack of fit	2.88E-04	9.59E-05	1.65	0.3128
Pure error	2.32E-04	5.81E-05		
Cor total	0.035			
R-squared	0.9853	Adeq precision	21.88	
Adj R-squared	0.9665	C.V. %	2.28	
Pred R-squared	0.8598	PRESS	4.97E-03	
(e) ANOVA results for optimization of MAF/Y (130)				
Model	0.04	4.40E-03	74.08	<0.0001
A spindle speed	1.08E-03	1.08E-03	18.12	0.0038
B feed rate	6.77E-04	6.77E-04	11.4	0.0118
C machining gap	4.58E-03	4.58E-03	77.07	<0.0001
AB	3.66E-05	3.66E-05	0.62	0.4583
AC	3.80E-06	3.80E-06	0.064	0.8076
BC	8.93E-05	8.93E-05	1.5	0.2599
A^2	0.021	0.021	349.09	<0.0001
B^2	1.72E-04	1.72E-04	2.89	0.1329
C^2	1.00E-02	1.00E-02	169.71	<0.0001
Residual	4.16E-04	5.94E-05		
Lack of fit	2.00E-04	6.66E-05	1.23	0.4078
Pure error	2.16E-04	5.41E-05		
Cor total	0.04			
R-squared	0.9896	Adeq precision	26.323	
Adj R-squared	0.9763	C.V. %	2.03	
Pred R-squared	0.9117	PRESS	3.53E-03	
(f) ANOVA results for optimization of MAF/Y (140)				
Model	0.037	4.12E-03	53.8	<0.0001
A spindle speed	1.01E-03	1.01E-03	13.21	0.0083
B feed rate	6.63E-04	6.63E-04	8.64	0.0217
C machining gap	3.85E-03	3.85E-03	50.29	0.0002
AB	4.49E-05	4.49E-05	0.59	0.4691
AC	1.00E-04	1.00E-04	1.3	0.2909
BC	1.88E-04	1.88E-04	2.45	0.1616
A^2	0.02	0.02	261	<0.0001
B^2	1.48E-04	1.48E-04	1.93	0.2072
C^2	9.10E-03	9.10E-03	118.67	<0.0001
Residual	5.37E-04	7.67E-05		
Lack of fit	3.38E-04	1.13E-04	2.27	0.2223
Pure error	1.99E-04	4.96E-05		
Cor total	0.038			
R-squared	0.9857	Adeq precision	21.387	
Adj R-squared	0.9674	C.V. %	2.29	
Pred R-squared	0.8481	PRESS	5.72E-03	

^aANOVA results for optimization of MAF/Y(90)^bANOVA results for optimization of MAF/Y (100)^cANOVA results for optimization of MAF/Y (110)^dANOVA results for optimization of MAF/Y (120)^eANOVA results for optimization of MAF/Y (130)^fANOVA results for optimization of MAF/Y (140)

Table 7 Diagnosis of model reliability

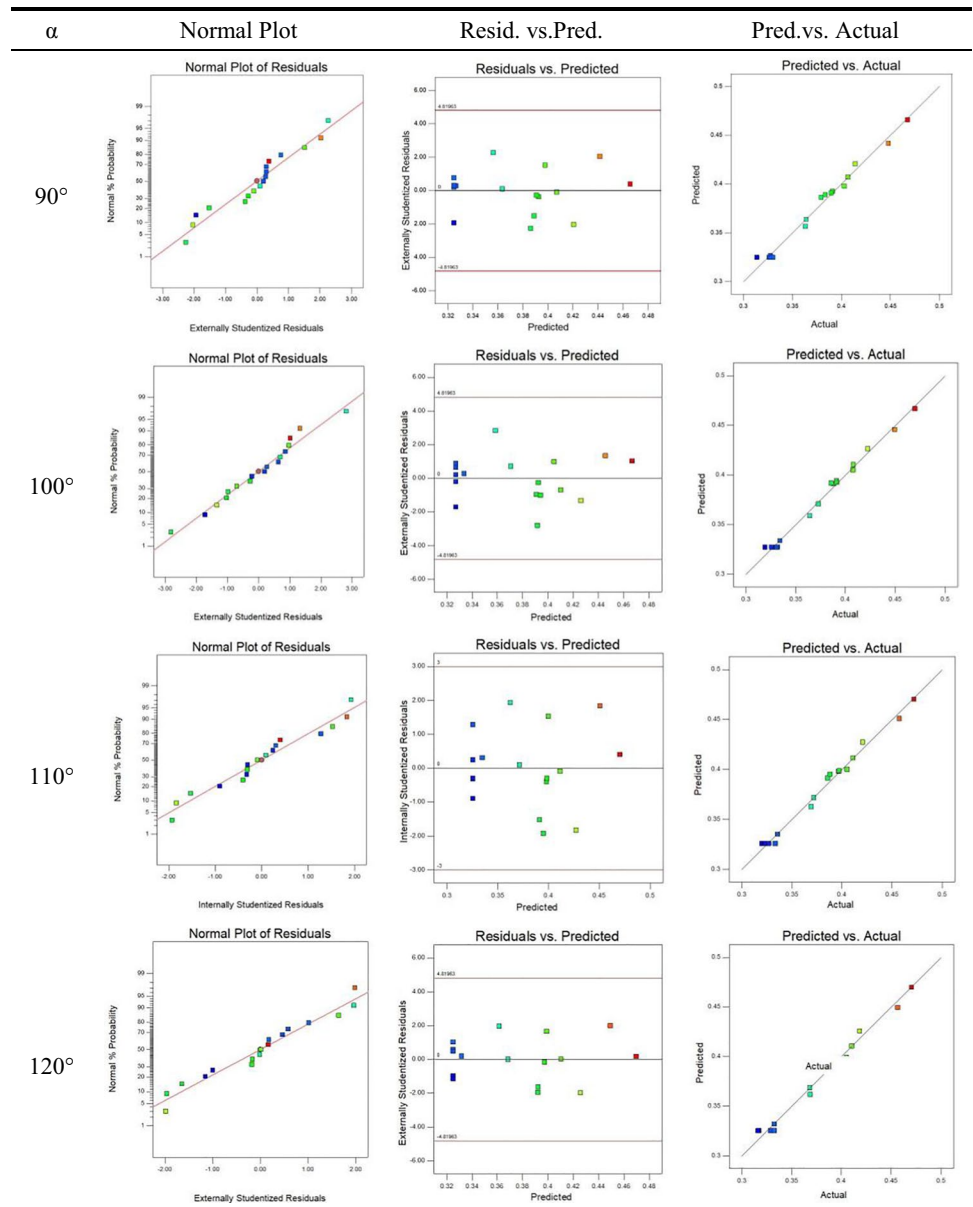


Table 7 (continued)

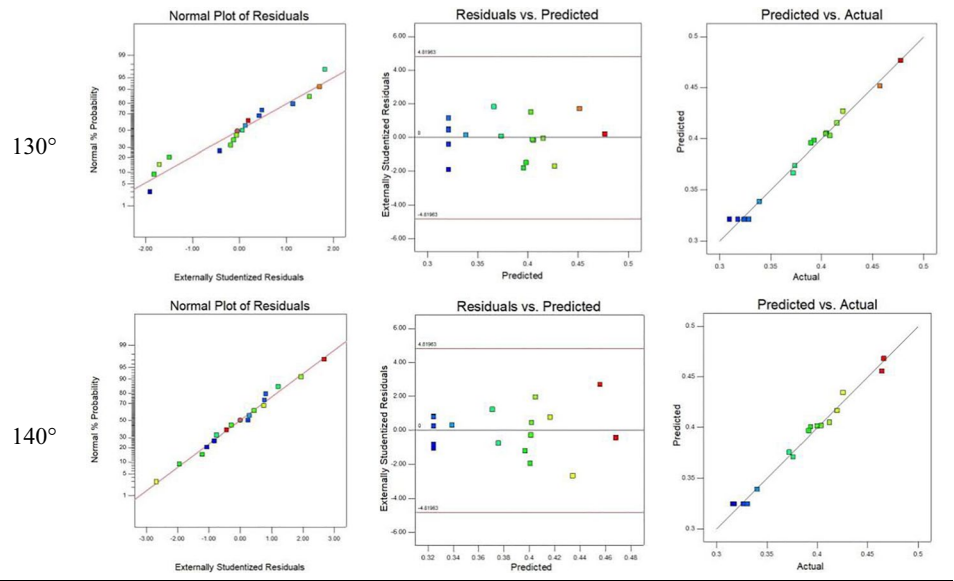
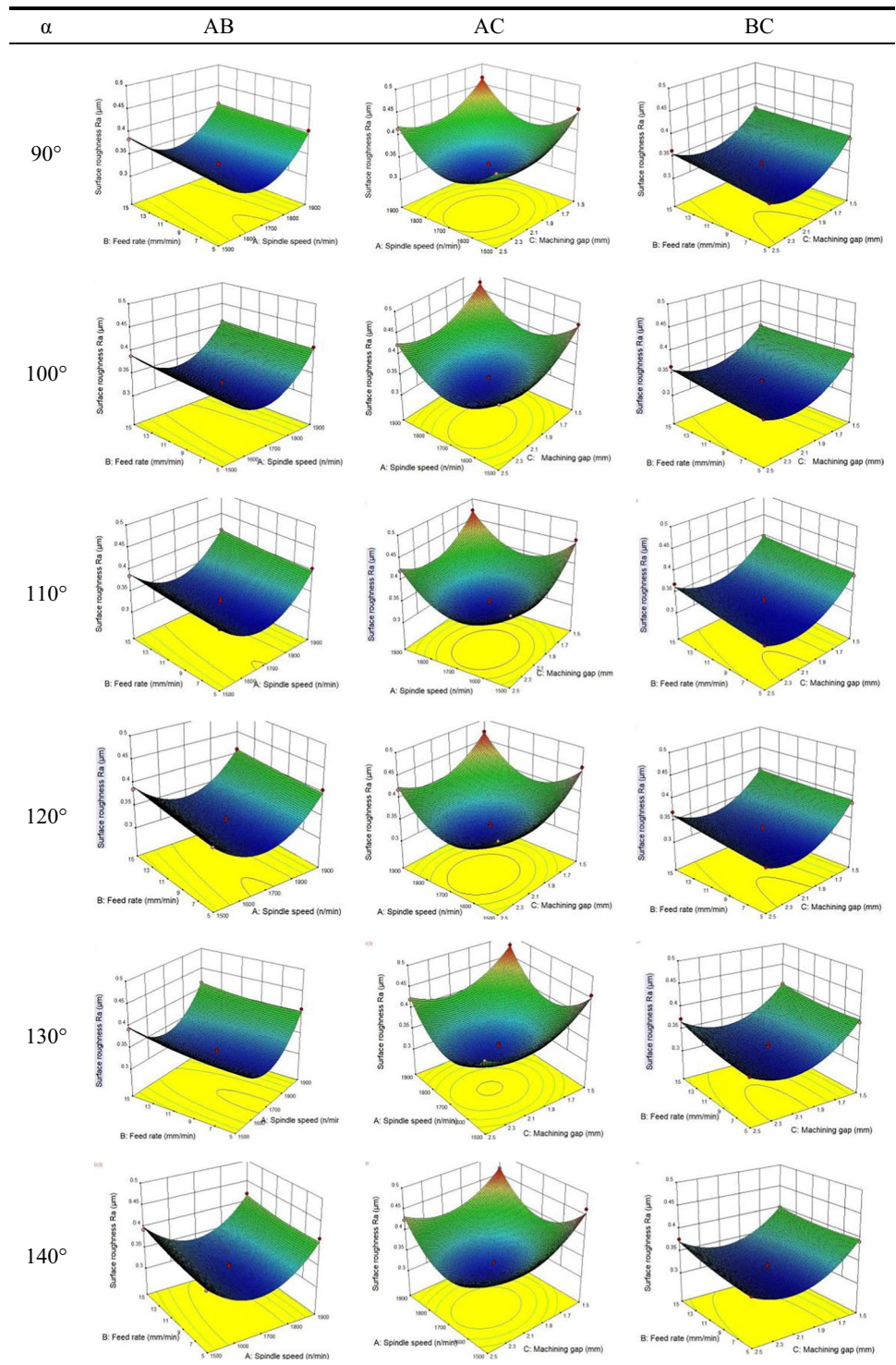


Table 8 The interactive effect of spindle speed (A), feed rate (B), and machining gap (C)



Author contributions Peixin Zhu contributed to the investigation, conduction of SLM and MAF experiments and writing of the original draft, writing of the review, and editing.

Guixiang Zhang contributed to the writing of the review, editing, and funding acquisition.

Xiao Teng contributed to the conduction of the SLM experiment and writing of the review, and editing.

Jiajing Du, Linzhi Jiang, Haoxin Chen, and Ning Liu contributed to the review and editing with the order provided.

Funding This work is supported by the National Natural Science Foundation of China (No. 51675316).

Data and material availability The data and materials set supporting the results of this article are included in the ending of the text.

Declarations

Ethics approval Not applicable.

Consent to participate The manuscript has been read and approved by all named authors.

Consent to publish All the authors listed in the manuscript have approved the manuscript will be considered for publication in The International Journal of Advanced Manufacturing Technology.

Competing interests The authors declare no competing interests.

References

- Jung J-G, Lee S-H, Cho Y-H, Yoon W-H, Ahn T-Y, Ahn Y-S, Lee J-M (2017) Effect of transition elements on the microstructure and tensile properties of Al–12Si alloy cast under ultrasonic melt treatment. *J Alloy Compd* 712:277–287. <https://doi.org/10.1016/j.jallcom.2017.04.084>
- Jung J-G, Ahn T-Y, Cho Y-H, Kim S-H, Lee J-M (2018) Synergistic effect of ultrasonic melt treatment and fast cooling on the refinement of primary Si in a hypereutectic Al–Si alloy. *Acta Mater* 144:31–40. <https://doi.org/10.1016/j.actamat.2017.10.039>
- Gayle FW, Goodway M (1994) Precipitation hardening in the first aerospace aluminum alloy: the Wright flyer crankcase. *Science* 266(5187):1015–1017. <https://doi.org/10.1126/science.266.5187.1015>
- Aamir M, Giasin K, Tolouei-Rad M, Vafadar A (2020) A review: drilling performance and hole quality of aluminium alloys for aerospace applications. *J Market Res* 9(6):12484–12500. <https://doi.org/10.1016/j.jmrt.2020.09.003>
- Starke EA, Staley JT (2011) Application of modern aluminium alloys to aircraft. *Fundam Aluminium Metall* 747–783. <https://doi.org/10.1533/9780857090256.3.747>
- Yan M, Wu X, Zhu Z (2003) Recent progress and prospects for aeronautical material technologies. *Aeronaut Manuf Technol* (12):19–25. https://kns.cnki.net/kcms/detail/detail.aspx?FileN_ame=HKGJ200312004&DbName=CJFQ2003
- Hull CW (1986) Apparatus for production of three-dimensional objects by stereolithography. US Patent No. 4575330
- Brandl E, Heckenberger U, Holzinger V, Buchbinder D (2012) Additive manufactured AlSi10Mg samples using selective laser melting (SLM): microstructure, high cycle fatigue, and fracture behavior. *Mater Des* 34:159–169. <https://doi.org/10.1016/j.matdes.2011.07.067>
- Bhaduria D, Pencheva P, Batala A et al (2017) Laser polishing of 3D printed mesoscale components. *Appl Surf Sci* 405:29–46. <https://doi.org/10.1016/j.apsusc.2017.01.211>
- Olakanmi EO, Cochrane RF, Dalgarno KW (2015) A review on selective laser sintering/melting (SLS/SLM) of aluminium alloy powders: processing, microstructure, and properties. *Prog Mater Sci* 74:401–477. <https://doi.org/10.1016/j.pmatsci.2015.03.002>
- Pyka G, Burakowski A et al (2012) Surface modification of Ti6Al4V open porous structures produced by additive manufacturing. *Adv Eng Mater* 14(6):363–370. <https://doi.org/10.1002/adem.201100344>
- Gao H, Peng C, Wang X (2019) Research progress on surface finishing technology of aeronautical complex structural parts manufactured by additive manufacturing. *Aeronaut Manuf Technol* 62(09):14–22. <https://doi.org/10.16080/j.issn1671-833x.2019.09.014>
- Leon A, Aghion E (2017) Effect of surface roughness on corrosion fatigue performance of AlSi10Mg alloy produced by selective laser melting (SLM). *Mater Charact* 131:188–194. <https://doi.org/10.1016/j.matchar.2017.06.029>
- Beaucamp AT, Namba Y, Charlton P, Jain S, Graziano AA (2015) Finishing of additively manufactured titanium alloy by shape adaptive grinding (SAG). *Surface Morphol Metrol Properties* 3(2):024001. <https://doi.org/10.1088/2051-672X/3/2/024001>
- Pyka G, Kerckhofs G, Papanitiou I, Speirs M, Schrooten J, Wevers M (2013) Surface roughness and morphology customization of additive manufactured open porous Ti6Al4V structures. *Materials* 6(10):4737–4757. <https://doi.org/10.3390/ma6104737>
- Dong G, Marleau-Finley J, Zhao YF (2019) Investigation of electrochemical post-processing procedure for Ti-6Al-4V lattice structure manufactured by direct metal laser sintering (DMLS). *Int J Adv Manuf Technol* 104:3401–3417. <https://doi.org/10.1007/s00170-019-03996-5>
- Peng C, Youzhi Fu, Wei H, Li S, Wang X, Gao H (2018) Study on improvement of surface roughness and induced residual stress for additively manufactured metal parts by abrasive flow machining. *Procedia CIRP* 71:386–389. <https://doi.org/10.1016/j.procir.2018.05.046>
- Bhaduri D, Ghara T, Penchev P, Paul S, Pruncu CI, Dimov S, Morgan D (2021) Pulsed laser polishing of selective laser melted aluminium alloy parts. *Appl Surf Sci* 558:149887. <https://doi.org/10.1016/j.apsusc.2021.149887>
- Zhu P, Zhang G, Jiajing Du, Jiang L, Zhang P, Cui Y (2021) Removal mechanism of magnetic abrasive finishing on aluminum and magnesium alloys. *Int J Adv Manuf Technol* 114:1717–1729. <https://doi.org/10.1007/s00170-021-06952-4>
- Yamaguchi H, Fergani O, Pei-Ying Wu (2017) Modification using magnetic field-assisted finishing of the surface roughness and residual stress of additively manufactured components. *CIRP Ann* 66(01):305–308. <https://doi.org/10.1016/j.cirp.2017.04.084>
- Guo J, KaHing Au, Sun C-N, Goh MH, Kum CW, Liu K, Wei J, Suzuki H, Kang R (2019) Novel rotating-vibrating magnetic abrasive polishing method for double-layered internal surface finishing. *J Mater Process Technol* 264:422–437. <https://doi.org/10.1016/j.jmatprotec.2018.09.024>
- Zhang J, Chaudhari A, Wang H (2019) Surface quality and material removal in magnetic abrasive finishing of selective laser melted 316L stainless steel. *J Manuf Process* 45:710–719. <https://doi.org/10.1016/j.jmapro.2019.07.044>
- Zeng J, Chen Y, Tan Y, Liu S (2018) Magnetic abrasive finishing of aero engine fuel Injection tube based on 3D printing. *Surf Technol* 47(09):296–302. <https://doi.org/10.16490/j.cnki.issn.1001-3660.2018.09.039>

24. Zhang G, Zhao Y, Zhao D, Yin F, Zhao Z (2011) Preparation of white alumina spherical composite magnetic abrasive by gas atomization and rapid solidification. *Scripta Mater* 65(5):416–419. <https://doi.org/10.1016/j.scriptamat.2011.05.021>
25. Teng X, Zhang G, Liang J, Li H, Liu Q, Cui Y, Cui T, Jiang L (2019) Parameter optimization and microhardness experiment of AlSi10Mg alloy prepared by selective laser melting. *Mater Res Express* 06(08):086592. <https://doi.org/10.1088/2053-1591/ab18d0>
26. Spierings AB, Schneider M, Eggenberger R (2011) Comparison of density measurement techniques for additive manufactured metallic parts. *Rapid Prototyp J* 17(5):380–386. <https://doi.org/10.1108/13552541111156504>
27. Arunangsu D, Susenjit S, Malobika K, Goutam S (2018) Application of Box–Behnken design and response surface methodology for surface roughness prediction model of CP-Ti powder metallurgy components through WEDM. *J Inst Eng (India) Ser D* 99:9–21. <https://doi.org/10.1007/s40033-017-0145-0>
28. Ma Z, Zhang K, Ren Z, Zhang DZ, Tao G, Haisheng Xu (2020) Selective laser melting of Cu–Cr–Zr copper alloy: parameter optimization, microstructure and mechanical properties. *J Alloy Compd* 828:154350. <https://doi.org/10.1016/j.jallcom.2020.154350>
29. Kwak J-S (2005) Application of Taguchi and response surface methodologies for geometric error in surface grinding process. *Int J Mach Tools Manuf* 45(3):327–334. <https://doi.org/10.1016/j.ijmachtools.2004.08.007>

Publisher's note Springer Nature remains neutral with regard to jurisdictional claims in published maps and institutional affiliations.